

# NiFe<sub>2</sub>O<sub>4</sub>/ZrO<sub>2</sub> Core-Shell Nanoparticles for Hydrogen Generation from Thermochemical Water-Splitting Process

Vinod Amar, Joseph Houck, Bharath Maddipudi and Rajesh Shende\*

Department of Chemical and Biological Engineering, South Dakota School of Mines & Technology, South Dakota, USA

## Abstract

A significant number of studies report synthesis of different redox materials and their performance evaluation for thermochemical water-splitting or water/CO<sub>2</sub>-splitting for H<sub>2</sub> or syngas production. As temperatures of thermochemical water-splitting process is typically higher ( $\geq 1000^\circ\text{C}$ ), nanoparticles of redox materials (e.g. spinel ferrites) undergo sintering and grain growth and eventually lose their reactivity that reflects into decrease in hydrogen volume generation with increase in number of thermochemical cycles. Among the redox materials reported so far, the information on the synthesis of core-shell nanoparticles (CSNs) and their use for thermochemical water-splitting process is meagre. This study reports synthesis of the Ni-ferrite/ZrO<sub>2</sub> CSNs using surfactant templating assisted sol-gel method. As-prepared gels with varying Ni-ferrite to Zr-precursor weight ratio of 1:5, 1:10 and 1:25 were aged, dried and calcined at 600°C. As-prepared powdered materials were characterized using powdered x-ray diffraction (XRD), BET specific surface area analyzer and transmission electron microscopy (TEM) and used as a packed-bed in an Inconel tubular reactor to determine hydrogen volume generation from the thermochemical-water splitting process. Hydrogen and oxygen generation capability of CSNs was determined by performing 5 consecutive thermochemical cycles at material regeneration and water-splitting reaction temperatures of 1100°C and 900°C, respectively. CSNs prepared with Ni-ferrite to Zr-precursor weight ratio of 1:10 showed the avg. porous ZrO<sub>2</sub> shell thickness of 3.24 nm and this material generated higher average H<sub>2</sub> volume.

**Keywords:** NiFe<sub>2</sub>O<sub>4</sub>/ZrO<sub>2</sub>, Core-shell nanoparticles (CSNs), Sol-gel, Thermochemical water-splitting, Hydrogen

## Introduction

Core-shell nanoparticles (CSNs) have attracted the scientific community with their diverse applications [1] in the areas of catalysis [2], energy generation/storage [3], drug delivery [4], optoelectronics [5], biosensors/bioimaging [4,6], electromagnetic waveguides [7], fuel cells [8], dye-sensitized solar cells [9] etc. Often, the synthesis of CSNs involves complex chemical reactions and selection of specific materials to overcome challenges [1,10] associated with compatibility, multi-functionality, surface characteristics and interfacial properties. Although a variety of CSNs such as TiO<sub>2</sub>(B)/CoP [11], CdS/BN [12], Fe<sub>2</sub>O<sub>3</sub>/ZnS/CdS [13] and ZnIn<sub>2</sub>S<sub>4</sub>/CuInS<sub>2</sub> [14] have been reported for photocatalytic hydrogen generation, the information on the synthesis of CSNs [15] of the redox materials and their use for thermochemical water-splitting for hydrogen production is extremely meagre. Many studies report synthesis of different iron based redox materials [16-22] and their performance evaluation for thermochemical water-splitting or water/CO<sub>2</sub>-splitting for H<sub>2</sub> or syngas production. As temperature of thermochemical water-splitting process is typically higher ( $\geq 1000^\circ\text{C}$ ) [23,24], nanoparticles of redox materials undergo sintering and lose reactivity [15]. It may be possible to mitigate sintering/grain-growth [16, 25-27] using nanoparticles with a core-shell morphology where a redox material can be placed at the core and enclosed within a thermally stable ceramic porous shell. With the use of such CSNs for thermochemical water-splitting process, stable hydrogen volume generation could be achieved at higher temperatures during multiple thermochemical cycles [28] because of the mitigation of possible sintering. From application viewpoint, it can be further stored as a compressed fluid [29], physical and chemical carriers such as metal organic frameworks (MOFs), carbon nanotubes, graphene, metal hydrides, alanates, and ammonia borane [30] or utilized directly in a hydrogen fuel cell (HFC) system for electrical energy production [31].

Over the past decade, significant progress has been made in using metal oxides as efficient redox materials [24,32-38] for a two-step thermochemical water-splitting process where in step-1, redox material is partially reduced at temperatures of  $< 1500^\circ\text{C}$  leading to oxygen release from crystal lattice and during step-2, oxygen from steam is scavenged by the partially reduced material leading to hydrogen generation at lower or

\***Correspondence to:** Prof. Rajesh Shende, Ph.D, Department of Chemical and Biological Engineering, South Dakota School of Mines & Technology, Rapid City, South Dakota, 57701-3995 USA. Tel: +1 605-394-1231; Fax: +1 605-394-1232; E-mail: Rajesh.Shende@sdsmt.edu

**Citation:** Amar V, Houck J, Maddipudi B, Shende R (2020) NiFe<sub>2</sub>O<sub>4</sub>/ZrO<sub>2</sub> Core-Shell Nanoparticles for Hydrogen Generation from Thermochemical Water-Splitting Process. *J Catal Chem Eng Adv* 7(1): 105. DOI: <https://doi.org/10.47275/2693-7182-105>.

**Received:** June 21, 2020; **Accepted:** August 03, 2020; **Published:** August 05, 2020

**Copyright:** © 2020 Amar V, et al. This is an Open Access article distributed under the terms of the Creative Commons Attribution 4.0 International License (CC-BY) (<http://creativecommons.org/licenses/by/4.0/>) which permits commercial use, including reproduction, adaptation, and distribution of the article provided the original author and source are credited.

similar temperatures. It is believed that these reactions are limited by the oxygen diffusion through a crystal lattice. Ni-ferrite in its spinel form has a stable crystal structure with high level of stability and recyclability. Due to these unique properties, several researchers have investigated NiFe<sub>2</sub>O<sub>4</sub> in addition to other classes of redox materials for hydrogen generation [32,39-46]. Bhosale et al. [47] have performed 125 thermochemical cycles using NiFe<sub>2</sub>O<sub>4</sub> and observed average hydrogen generation volume of 2.22 mL/g/cycle, which was higher as compared to other ferrites of Mn, Zn, Co and Mg. Due to high temperature multiple thermochemical cycling [42,48,49], redox materials undergo thermal fatigue and morphological changes leading to grain growth and sintering. To address these issues, approaches such as incorporation of chemically different moieties in a crystal lattice, admixing with ceramic nanoparticles [50], CSNs of redox and ceramic materials [15] and atomic layer deposition could be noticed in the published literature [43,51,52]. In one of our studies, we reported synthesis of NiFe<sub>2</sub>O<sub>4</sub>/Y<sub>2</sub>O<sub>3</sub> core-shell nanoparticles via sol-gel technique [53] and observed similar H<sub>2</sub> volume generation during 5 thermochemical cycles performed at 900-1100°C. However, achieving the mono-particulate dispersion and controlling the shell thickness were challenging to accomplish synthesis of CSNs.

Several researchers have attempted to synthesize the CSNs via solvothermal reaction [54], one step alkoxide hydrolysis method [55], sol-gel synthesis [15,53,56], polymeric precursor method [57] and colloidal route [58]. While synthesizing NiFe<sub>2</sub>O<sub>4</sub>/Y<sub>2</sub>O<sub>3</sub> CSNs, we observed some merits with the sol-gel technique, which allowed better flexibility in terms of the shell thickness and porosity. Analysis of ceramic interface with redox material suggest that the bonding strength of the ceramics and metal oxide interface at microstructural level is higher for cubic ZrO<sub>2</sub> [59,60]. The phase transformations [61] of ZrO<sub>2</sub> in its monoclinic, tetragonal, and cubic forms are found to be thermally stable upto 1170°C, 2370°C and 2706°C, respectively. Thus, NiFe<sub>2</sub>O<sub>4</sub> nanoparticles encapsulated inside a porous shell of ZrO<sub>2</sub> can possibly prevent grain-growth or sintering and generate stable H<sub>2</sub> volume generation during multiple thermochemical cycling.

In this study, we used pluronic P123 assisted sol-gel technique to synthesize NiFe<sub>2</sub>O<sub>4</sub>/ZrO<sub>2</sub> CSNs, which were characterized by powdered X-ray diffraction, BET surface area analysis and transmission electron microscopy (TEM). CSNs were loaded as packed-bed in Inconel tubular reactor and their hydrogen generation capability was determined at 900°-1100 °C during 5 consecutive thermochemical cycles.

## Experimental

### Materials

Nickel chloride (NiCl<sub>2</sub>·6H<sub>2</sub>O, 98%), iron chloride (FeCl<sub>2</sub>·4H<sub>2</sub>O, 99%), ethanol (C<sub>2</sub>H<sub>5</sub>OH, 95%) and propylene oxide (C<sub>3</sub>H<sub>6</sub>O, 99%) were purchased from Alfa Aesar, MA, USA. Zirconium (IV) isopropoxide solution (70 wt.% in 1-propanol) and pluronic P123 were purchased from Sigma Aldrich, MO, USA. All chemicals were used as received. Quartz wool was used as a supporting material for the packed-bed of CSNs and it was purchased from Wale Apparatus Co. Inc., PA, USA. High temperature raschig rings (6 mm I.D.) from Brewhaus Corporation, TX, USA were used for supporting the packed-bed of CSNs. Ultra-high purity (99.99 %) N<sub>2</sub> was purchased from Matheson Linweld, SD, USA. Thermochemical water-splitting step was carried out using deionized water.

### Synthesis of Ni-ferrite/ ZrO<sub>2</sub> core-shell nanoparticles (CSNs)

NiCl<sub>2</sub>·6H<sub>2</sub>O and FeCl<sub>2</sub>·4H<sub>2</sub>O precursors in the wt. ratio of 1:2 was added in ethanol and sonicated for 90 min, until a visually clear dispersion was obtained. Upon propylene oxide addition, the gel was obtained, which was calcined as per the procedure reported elsewhere [62]. Sol-gel derived Ni-ferrite powder was placed in isopropanol and sonicated for 2 hours. To this dispersion, 10 wt.% pluronic P123 surfactant was added and the dispersion was further sonicated for 2 hours. Next, zirconium (IV) isopropoxide (70% dispersion in IPA) was added drop wise to the previously made dispersion of Ni-ferrite nanoparticles in isopropanol. Addition of Zr-precursor was performed at 3 concentration levels with expected yields of ZrO<sub>2</sub> in Ni-ferrite/ZrO<sub>2</sub> powder as 5, 10 and 25 wt%. Followed by Zr-precursor addition, the resultant dispersion was further sonicated for 2 hours to achieve surface coating of precursor molecules on N-ferrite nanoparticles. Addition of de-ionized water resulted in a gel, which was aged for 48 hours and dried overnight at 50°C. Dried gel was calcined at 600°C to obtain powdered material. The entire synthesis route for Ni-ferrite/ZrO<sub>2</sub> CSNs is shown in figure 1, which also provides specific information about the calcination conditions.

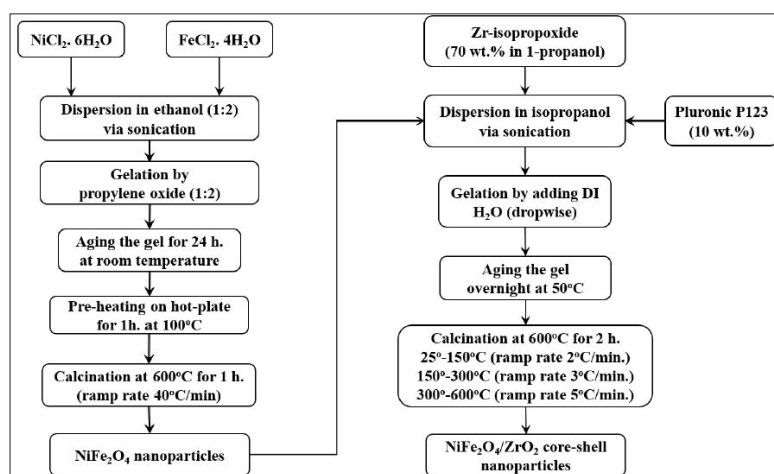


Figure 1: Sol-gel synthesis route for the NiFe<sub>2</sub>O<sub>4</sub>/ZrO<sub>2</sub> core-shell nanoparticles.

## Characterization of Ni-ferrite/ ZrO<sub>2</sub> core-shell nanoparticles (CSNs)

### Powdered x-ray diffraction (XRD)

Ni-ferrite/ ZrO<sub>2</sub> CSNs were analyzed for phase composition and crystallographic properties using Rigaku Ultima-Plus X-ray diffractometer provided with CuK $\alpha$  radiation ( $\lambda = 1.5406 \text{ \AA}$ , 40 kV, 40 mA). The phase composition was analysed in the range of  $10^\circ \leq 2\theta \leq 70^\circ$  at scanning speed of  $1^\circ$  per minute using reference intensity ratio (RIR) method.

### BET specific surface area analysis

As prepared Ni-ferrite/ ZrO<sub>2</sub> powdered material of CSNs was degassed at 200°C for 1 hour and analyzed for specific surface area and pore volume using the micromeritics Gemini II-2375 BET (Brunauer-Emmett-Teller) surface area analyzer.

### Transmission electron microscopy (TEM)

As-calcined powdered material was sonicated in ethanol for 2 hours and this dispersion was added onto the carbon coated copper grids, which were further plasma cleaned to remove the impurities. Powdered sample loaded onto a carbon coated copper grid was analyzed by the Hitachi H-7000 FA transmission electron microscope to analyze the morphology of the CSNs.

### Packed-bed reactor set-up and procedure for thermochemical cycling

Packed-bed tubular reactor set-up for the thermochemical water-splitting process is schematically shown in figure 2. The main parts of the reactor set-up includes: high temperature vertical split furnace (Verder Scientific, Inc., Carbolite Gero USA Inc., PA, USA) provided with *k*-type thermocouple and PID controller, Inconel 718 tubular reactor (I.D. 0.86 inch and length 26 inch), water vaporizing set-up consisted of a peristaltic pump (Fluid Metering Inc.,) and low-temperature horizontal tube furnace (Carbolite Inc., USA), mass flow meter (AALBORG Inc., USA) mounted on the reactor feed line, UHP grade (99.99% purity) N<sub>2</sub> cylinder to supply a carrier fluid, pre-calibrated hydrogen sensor (HY-OPTIMA 700 series, H2SCAN, CA, USA) and oxygen sensor (Advanced Instruments Inc., CA, USA) installed on reactor outlet lines and computer interface for the data acquisition. Ni-ferrite/ZrO<sub>2</sub> CSNs as powder was packed in the middle section of the Inconel tubular reactor with high temperature raschig rings (Brewhaus America, Inc., TX, USA) and glass wool (McMaster-Carr, IL, USA) as support materials. Two moisture adsorption columns loaded with drierite, anhydrous calcium sulfate (W.A.Hammond Drierite Company Inc., OH, USA) and a tubular condenser was installed on the exit line of the reactor outlet to remove moisture and lower down the temperature of the product gas stream. Additional details of the thermochemical reactor set-up can be found elsewhere [27,38,63-65].

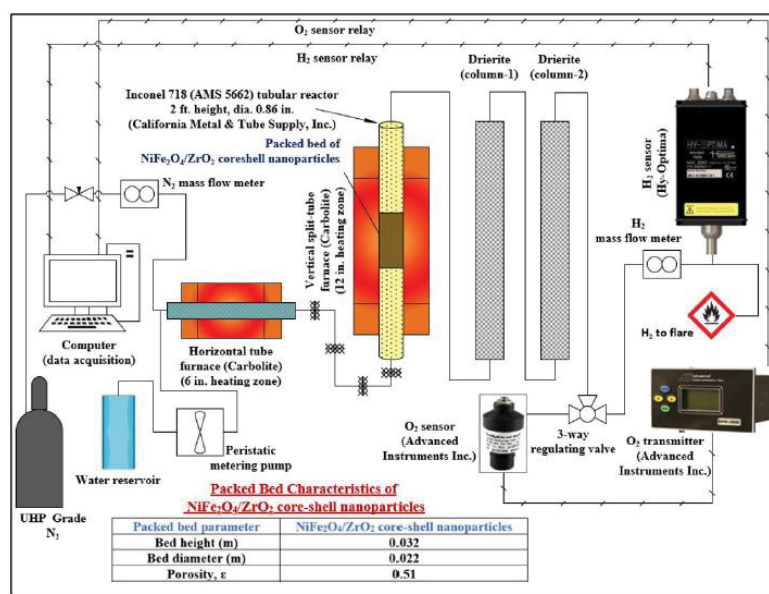


Figure 2: Schematic of thermochemical water-splitting set-up utilizing a packed-bed of NiFe<sub>2</sub>O<sub>4</sub>/ZrO<sub>2</sub> core-shell nanoparticles (CSNs) for hydrogen generation.

To perform a regeneration step, the packed-bed of CSNs was heated to 1100°C and maintained for arbitrary time of 2 hours. During this step, N<sub>2</sub> carrier gas flow rate was maintained at the rate of 35 SCCM. The oxygen sensor installed on the reactor outlet lines provided the oxygen concentration in the product stream. For the water-splitting step, the temperature of the reactor was lowered down to 900°C and de-ionized water was pumped through water-vaporizing set-up, which supplied the steam to the packed-bed tubular reactor at 500°C. The product gas was monitored via hydrogen sensor mounted on the reactor exit lines. As soon as hydrogen concentration reaches 0.5% in the product gas, steam was stopped and the packed-bed was regenerated again at 1100°C for 2 hours for next water-splitting step. During the water splitting step, the product gas stream from the sensor outlet was directed to the flare as a safety precaution. Five consecutive thermochemical cycles were performed and transient profiles were recorded. Numerical integration of the data obtained from the transient profiles provided the hydrogen volume. Hydrogen

sensor (HY-OPTIMA 700 series, H2SCAN, CA, USA) output of hydrogen volume was validated with Agilent 7890 gas-chromatography (GC). The parameters used for GC analysis of hydrogen in product gas were: column- chompak capillary column (25 m × 0.53 mm), detector- TCD, oven temperature- 105 °C detector temperature- 250°C, and carrier gas- UHP N<sub>2</sub> with the flow rate of 5 ml/min.

## Results and Discussion

### X-Ray diffraction of Ni-ferrite/ ZrO<sub>2</sub> CSNs

The XRD patterns of as-calcined NiFe<sub>2</sub>O<sub>4</sub>/ZrO<sub>2</sub> CSNs prepared with different NiFe<sub>2</sub>O<sub>4</sub>: Zr-precursor weight ratios are shown in figure 3. The 2θ reflections corresponding to 32.32°, 35.70°, 37.32°, 43.38°, 53.92°, 57.36° and 63° indicate NiFe<sub>2</sub>O<sub>4</sub> spinel phase, which is consistent with the published literature [66-68] and ICDD (International Center for Diffraction Data) pattern. Three characteristic peaks observed at 2θ reflections of 30.22°, 50.39° and 60.06°, which correspond to miller indices of (111), (220) and (311), respectively, were observed to be for tetragonal ZrO<sub>2</sub>. These 2θ reflections agree to those reported by other investigators [69, 70] and also, found to be consistent with the ICDD pattern (JCPDS, No 17-0923) [71]. XRD patterns of the powdered materials prepared with NiFe<sub>2</sub>O<sub>4</sub> to Zr-precursor weight ratios of 1:5, 1:10 and 1:25 indicated nominal phase composition (Table 1) of NiFe<sub>2</sub>O<sub>4</sub> (95.7 wt.%)/ ZrO<sub>2</sub> (4.3 wt.%), NiFe<sub>2</sub>O<sub>4</sub> (91.2 wt.%)/ ZrO<sub>2</sub> (8.8 wt.%), and NiFe<sub>2</sub>O<sub>4</sub> (73.8 wt.%)/ ZrO<sub>2</sub> (26.2 wt.%), respectively.

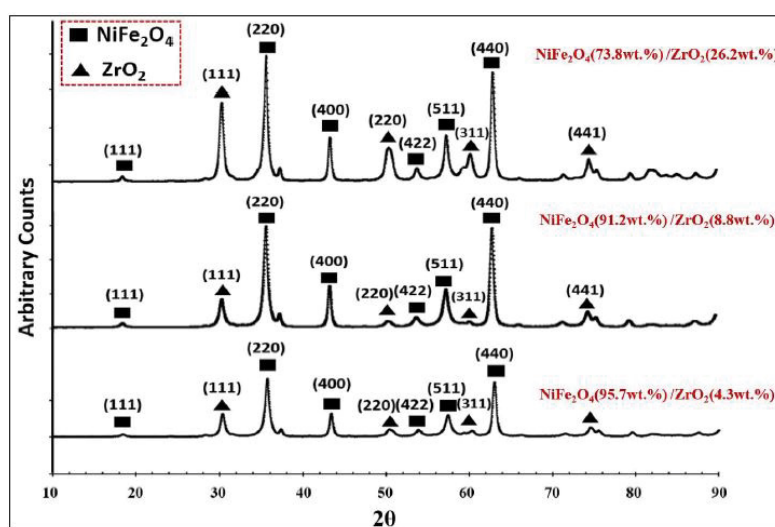


Figure 3: Powdered x-ray diffraction patterns of NiFe<sub>2</sub>O<sub>4</sub>/ZrO<sub>2</sub> (CSNs) prepared with different weight ratios of NiFe<sub>2</sub>O<sub>4</sub> to Zr-isopropoxide precursor.

Table 1: Nominal phase composition by XRD, specific surface area by BET analysis, and average shell thickness by TEM of the NiFe<sub>2</sub>O<sub>4</sub>/ZrO<sub>2</sub> CSNs synthesized using different NiFe<sub>2</sub>O<sub>4</sub>:Zr-precursor weight ratios and corresponding average H<sub>2</sub> volume generated.

NiFe <sub>2</sub> O <sub>4</sub> : Zr-precursor weight ratio	Phase composition by XRD	BET SSA, m <sup>2</sup> /g	ZrO <sub>2</sub> shell thickness from TEM, nm	Avg. H <sub>2</sub> volume generated, mL.g <sup>-1</sup> .cycle <sup>-1</sup> (2-5 thermochemical cycles)
1:05	NiFe <sub>2</sub> O <sub>4</sub> (95.7%), ZrO <sub>2</sub> (4.3%)	28.35	—	7.27
1:10	NiFe <sub>2</sub> O <sub>4</sub> (91.2%), ZrO <sub>2</sub> (8.8%)	34.32	3.24	7.28
1:25	NiFe <sub>2</sub> O <sub>4</sub> (73.8%), ZrO <sub>2</sub> (26.2%)	32.75	6.12	2.67

### BET specific surface area analysis of CSNs

Specific surface area (SSA) results of CSNs are also presented in table 1. SSA of Ni-ferrite/ ZrO<sub>2</sub> CSNs prepared with different Ni-ferrite: Zr-precursor weight ratios was found to be in the range of 28 to 34 m<sup>2</sup>/g whereas pore volume was observed as 0.08 to 0.227 cm<sup>3</sup>/g. It is believed that the use of pluronic P123 during sol-gel synthesis has induced the porosity [72, 73], which is desired for efficient mass transfer of the steam and yield of the product gas.

### TEM analysis of CSNs

The morphology of the NiFe<sub>2</sub>O<sub>4</sub>/ZrO<sub>2</sub> CSNs was investigated using JEOL Hitachi H-700 FA transmission electron microscope as per the procedure described in section 2.3.3. TEM images of NiFe<sub>2</sub>O<sub>4</sub> (91.2 wt.%)/ZrO<sub>2</sub> (8.8 wt.%), NiFe<sub>2</sub>O<sub>4</sub> (73.8 wt.%)/ ZrO<sub>2</sub> (26.2 wt.%) CSNs and atomic fringes with FFT (Fast Fourier Transform) analysis are presented in figure 4. The *d*-spacing of the core nanoparticle of 0.48 nm evidently confirmed NiFe<sub>2</sub>O<sub>4</sub> oriented along <111> plane, which is consistent with the *d*-spacing reported in the literature for NiFe<sub>2</sub>O<sub>4</sub>. TEM imaging revealed ZrO<sub>2</sub> shell thickness of 3.24 nm and 6.12 nm for NiFe<sub>2</sub>O<sub>4</sub> (91.2 wt.%)/ ZrO<sub>2</sub> (8.8 wt.%) and NiFe<sub>2</sub>O<sub>4</sub> (73.8 wt.%)/ZrO<sub>2</sub> (26.2 wt.%) CSNs, respectively. This indicates larger shell thickness for the CSNs prepared with the NiFe<sub>2</sub>O<sub>4</sub>: Zr-precursor weight ratio of 1:25. At higher weight ratio of 1:25, several agglomerated particles can be seen in figure 4c; HRTEM image shown here is from our previous work [50]. It is to be noted that addressing the issue of deagglomeration of nanoparticles could be critical in achieving core-shell morphology [53,74,75]. It is speculated that at this higher weight ratio of 1:25, undesirable ZrO<sub>2</sub> nanoparticles could be formed separately in addition to NiFe<sub>2</sub>O<sub>4</sub>/ZrO<sub>2</sub> CSNs. The possible route for the formation

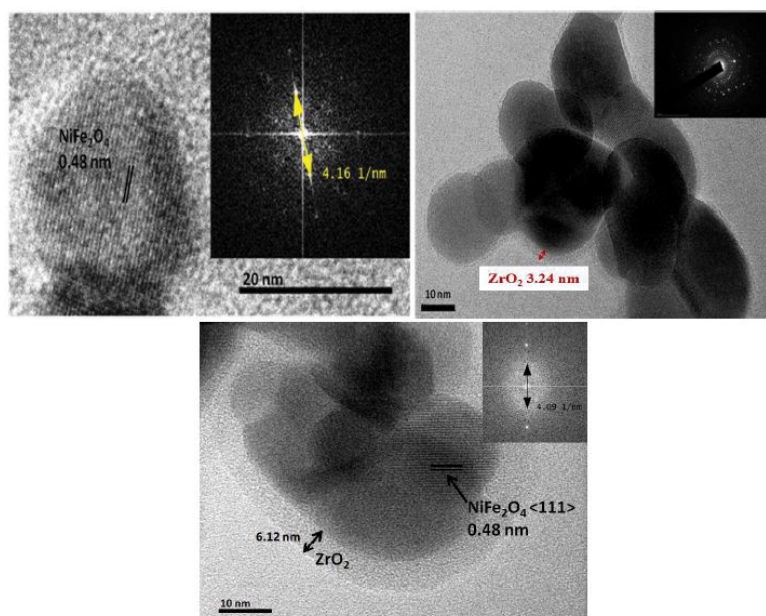


**Figure 4:** HRTEM images showing a) d-spacing corresponding to NiFe<sub>2</sub>O<sub>4</sub>, b) particle size and shell thickness of NiFe<sub>2</sub>O<sub>4</sub>/ZrO<sub>2</sub> CSNs prepared with 10 wt.% Zr-isopropoxide and c) multiple particles within the shell of NiFe<sub>2</sub>O<sub>4</sub>/ZrO<sub>2</sub> CSNs prepared with 25 wt.% Zr-isopropoxide.

of core-shell morphology using pluronic P123 and Zr-isopropoxide precursor is schematically shown in figure 5. The surfactant, pluronic P123 has hydrophobic poly (propylene oxide) (PPO) chain and hydrophilic poly (ethylene glycol) (PEG) chains forming poly (ethylene oxide) (PEO) linkage. When NiFe<sub>2</sub>O<sub>4</sub> powder is placed in ethanol containing pluronic P123, the surfactant is expected to interact with hydrophobic ferrite surface *via* weak van der Waal forces [76,77]. Upon addition of Zr-isopropoxide and water, hydrolysis and condensation reactions occur as shown in figure 5 leading to a macromolecular Zr-oxyhydroxide structured gel. Calcination of aged and dried gel at 600°C should decompose the pluronic P123 PPO and PEO chains and dehydrate Zr-oxyhydroxide leading to the formation of a porous ZrO<sub>2</sub> shell over the NiFe<sub>2</sub>O<sub>4</sub> nanoparticle at the core resulting in core-shell morphology.

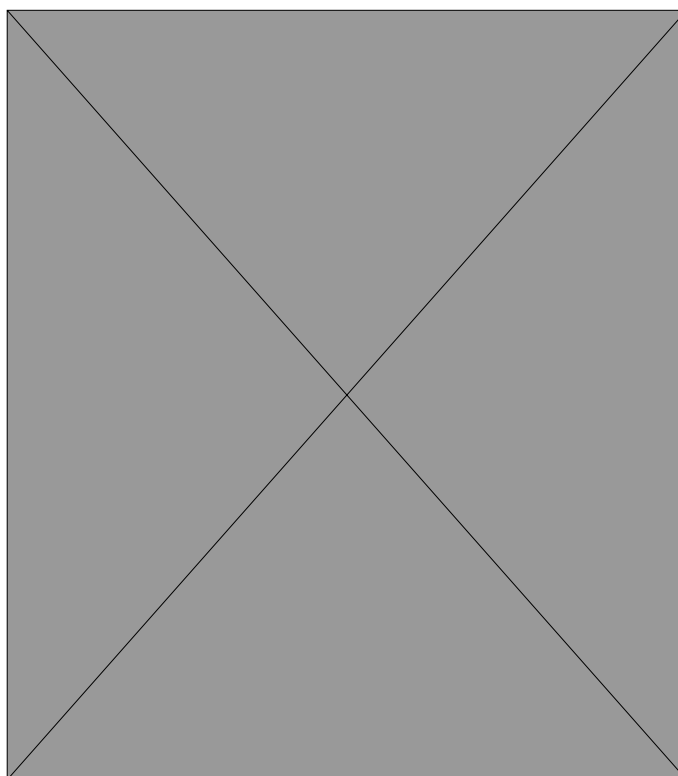


**Figure 5:** Schematic represents formation of NiFe<sub>2</sub>O<sub>4</sub>/ZrO<sub>2</sub> CSNs with hydrolysis and condensation reactions.

## Hydrogen and oxygen generation using NiFe<sub>2</sub>O<sub>4</sub>/ZrO<sub>2</sub> CSNs

Powdered material of NiFe<sub>2</sub>O<sub>4</sub>/ZrO<sub>2</sub> CSNs prepared with different weight ratios of NiFe<sub>2</sub>O<sub>4</sub>:Zr-precursor was individually loaded in Inconel tubular reactor and regeneration step was performed for 2 hours at 1100 °C as per the procedure outlined in section 2.4. During the regeneration step, oxygen concentration in the product gas was monitored using the oxygen sensor installed in the thermochemical water-splitting set-up as shown in figure 2. Followed by the regeneration step, temperature of the reactor was lowered to 900 °C and water-splitting step was performed. Hydrogen generated during the water-splitting step was continuously monitored and data was acquired using online hydrogen sensor as per the procedure outlined in section 2.4. Transient profiles obtained with different NiFe<sub>2</sub>O<sub>4</sub>/ZrO<sub>2</sub> CSNs are shown in figure 6. At first glance, stable hydrogen volume generation could be observed with NiFe<sub>2</sub>O<sub>4</sub> (73.8 wt.%)/ZrO<sub>2</sub> (26.2 wt.%) CSNs; however, the volume generated with this material is lower as compared with the other CSNs investigated in this study. For NiFe<sub>2</sub>O<sub>4</sub> (95.7 wt.%)/ZrO<sub>2</sub> (4.3 wt.%) CSNs, transient profiles show continuous decrease in hydrogen volume generation with increase in number of thermochemical cycles. For the CSNs prepared with NiFe<sub>2</sub>O<sub>4</sub>:Zr-precursor weight ratios of 1:5, we can expect very thin 1-2 nm ZrO<sub>2</sub> shell thickness as compared to 3.2 nm and 6.1 nm observed for the CSNs prepared with higher weight ratios of 1:10 and 1:25 (Table 1). Such a thin shell thickness may not be able to withstand thermal stresses caused by higher temperatures of thermochemical reaction. Consequently, shell can rupture leading to sintering/grain growth.

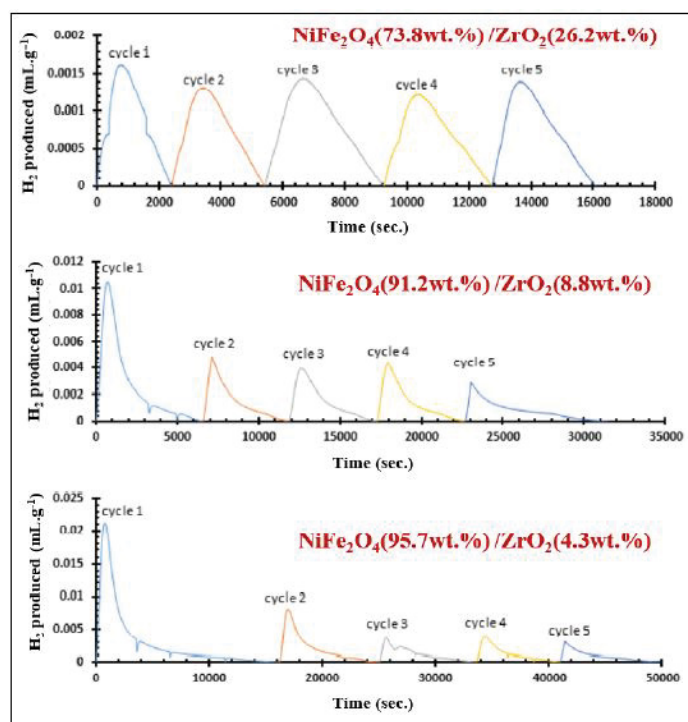


Figure 6: Transient hydrogen profiles obtained during five thermochemical cycles where water-splitting step was performed at 900°C using a packed-bed of NiFe<sub>2</sub>O<sub>4</sub>/ZrO<sub>2</sub> CSNs.

The data obtained from the transient profiles was numerically integrated using Simpson's rule to determine the hydrogen volume generated and the results obtained are shown in figure 7. It can be observed that as number of thermochemical cycles increase, hydrogen volume generation decrease with the core NiFe<sub>2</sub>O<sub>4</sub> nanoparticles. Possible phase transformation that can occur during the regeneration and water-splitting steps

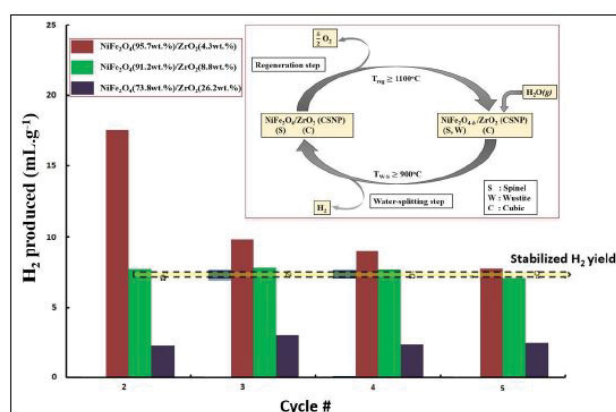
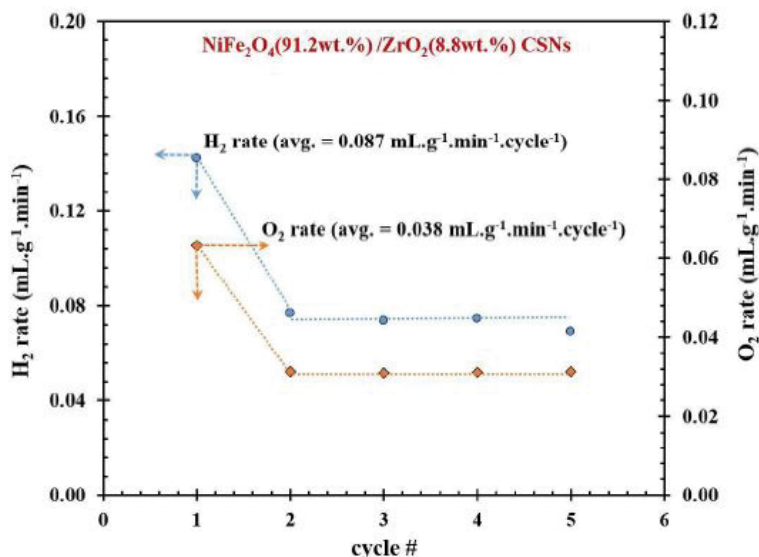


Figure 7: Hydrogen volume generated by a packed-bed of NiFe<sub>2</sub>O<sub>4</sub>/ZrO<sub>2</sub> CSNs during thermochemical cycles where water-splitting and regeneration steps were performed at 900°C and 1100°C, respectively; inset shows regeneration and water-splitting steps involving possible crystalline phase transformations.

for the CSNs is schematically shown as an inset in figure 7. In the CSNs, the crystalline phase of NiFe<sub>2</sub>O<sub>4</sub> and ZrO<sub>2</sub> is spinel (S) and cubic (C), respectively. During the regeneration step, the S phase is partially reduced leading to the formation of some fraction of a wustite (W) phase (Ni rich phase, Ni<sub>x</sub>Fe<sub>1-x</sub>O). The resultant crystalline phase mixture of S and W is reverted to S phase during the water-splitting step [25], wherein oxygen is scavenged from the steam producing hydrogen.

Several investigators demonstrated hydrogen generation using NiFe<sub>2</sub>O<sub>4</sub> and other ferrites at  $\geq 700$  °C [78] although stable hydrogen volume generation was observed at 1400°C [42]. Han et al [79] prepared several ferrites such as NiFe<sub>2</sub>O<sub>4</sub>, CuFe<sub>2</sub>O<sub>4</sub>, Ni 0.5 Mn 0.5 Fe<sub>2</sub>O<sub>4</sub> and Cu 0.5 Mn 0.5 Fe<sub>2</sub>O<sub>4</sub> via solid state synthesis route and performed 5 thermochemical cycles at 800-1200°C and reported hydrogen volume generation using thermo-gravimetric analysis (TGA)/differential thermal analysis (DTA) set-up. Among these materials, NiFe<sub>2</sub>O<sub>4</sub> showed a maximum average hydrogen volume generation. Furthermore, these investigators report that NiFe<sub>2</sub>O<sub>4</sub> showed the oxygen generation from 610 °C; however, rapid oxygen evolution was observed at 1150°C [76]. Tamaura et al [78] reports hydrogen volume generation of 5.5 ml/g from thermochemical water-splitting reaction with Ni 0.5 Mn 0.5 Fe<sub>2</sub>O<sub>4</sub> at 700°-1000°C, where hydrogen yield was determined using the mass spectroscopy. No appreciable hydrogen volume generation was noticed after 15 minutes of reaction time. It is believed that still higher temperatures may be required to achieve higher hydrogen yields. Zhai et al. [24] discovered a new class of polycation oxide (PCO), (FeMgCoNi) Ox and compared its H<sub>2</sub> evolution capability with CoFe<sub>2</sub>O<sub>4</sub>, NiFe<sub>2</sub>O<sub>4</sub>, and CeO<sub>2</sub> at regeneration temperatures of 1100°C and 1300°C, and water-splitting temperature of 800°C. H<sub>2</sub> yield, which was measured using inline TGA/GC, was found to be higher for PCO material as compared with ferrites and ceria. Saavedra et al [80] investigated commercial NiFe<sub>2</sub>O<sub>4</sub> powdered material and performed 8 thermochemical cycles at regeneration and water-splitting temperatures of 1450°C and 950°C, respectively and observed an average hydrogen volume of 11.46 ml/g using micro-gas chromatography (GC) technique. For the NiFe<sub>2</sub>O<sub>4</sub> nanoparticles, we have validated our hydrogen volume generation results from H2Scan sensor output with the GC as per the details provided in section 2.4; product gas sampling was performed periodically after every 15 min during the course of water-splitting reaction. Similar hydrogen volume generation was observed using the hydrogen sensor as well as GC. Among CSNs, NiFe<sub>2</sub>O<sub>4</sub> (91.2 wt.%) / ZrO<sub>2</sub> (8.8 wt.%) CSNs show stable hydrogen volume generation of 7.3 ml/g, 7.24 ml/g, 7.28 ml/g, and 7.3 ml/g during 2<sup>nd</sup>, 3<sup>rd</sup>, 4<sup>th</sup> and 5<sup>th</sup> thermochemical cycles, respectively with an average value of 7.3 ml/g/cycle at thermochemical cycling temperatures of 900°-1100°C. An average oxygen volume generated observed for these CSNs was 3.75 ml/g/cycle. At the temperatures of 900°-1100°C, NiFe<sub>2</sub>O<sub>4</sub>/ Y<sub>2</sub>O<sub>3</sub> core-shell nanoparticles generated average hydrogen and oxygen volumes of 7.48 ml/g and 4.08 ml/g, respectively [53] over 8 thermochemical cycles.

By considering the hydrogen volume generated over a period of certain time corresponding to each water-splitting step, rate of evolution was determined. In addition, the oxygen volume generated during each regeneration step of 2 hours was acquired using the oxygen sensor output. Both hydrogen and oxygen volume generation rates for NiFe<sub>2</sub>O<sub>4</sub> (91.2 wt.%) / ZrO<sub>2</sub> (8.8 wt.%) CSNs are shown in figure 8, which shows similar volume



**Figure 8:** Rate of hydrogen (H<sub>2</sub>) and oxygen (O<sub>2</sub>) generation by a packed-bed of NiFe<sub>2</sub>O<sub>4</sub>(91.2 wt.%) / ZrO<sub>2</sub>(8.8 wt.%) CSNs during 5 consecutive thermochemical cycles where water-splitting and regeneration steps were performed at 900°C and 1100°C, respectively.

generation rates for thermochemical cycles 2-5. Average hydrogen and oxygen volume generation rate of 0.087 ml/min/g/cycle and 0.038 ml/min/g/cycle, respectively, were observed during 5 consecutive thermochemical cycles. Lower rates could be attributed to the porous shell that could act as a barrier for number of diffusional processes such as steam carried by N<sub>2</sub> carrier gas (gas-film diffusion), gas-solid (ZrO<sub>2</sub> shell) interfacial diffusion, diffusion through porous shell layer reaching ZrO<sub>2</sub>/ NiFe<sub>2</sub>O<sub>4</sub> interface and diffusion through NiFe<sub>2</sub>O<sub>4</sub>. Diffusional limitations are also expected to exist during the regeneration step. If porous shell is sufficiently thick enough, thermal stabilization could be achieved to some extent by minimizing sintering of the CSNs. As thermal energy drives the grain boundaries, generally, the pore volume reduces and particles densify, which results in sintering of nanoparticles [81,82]. In the case of powdered mixtures of ferrite and ceramic nanoparticles, heterogeneous grain growth or sintering was observed [50], which was found to be mitigated by encapsulating ferrite nanoparticles within a porous thin shell of thermally

stable yttria [15]. In the case of NiFe<sub>2</sub>O<sub>4</sub>/ZrO<sub>2</sub> CSNs, it is believed that a porous shell of ZrO<sub>2</sub> acted as a physical barrier preventing grain growth of NiFe<sub>2</sub>O<sub>4</sub> nanoparticles leading to thermal stabilization.

## Conclusion

Ni-ferrite/ ZrO<sub>2</sub> powdered material prepared by pluronic P123 templating assisted sol-gel method showed core-shell morphology in TEM imaging. From lattice fringes, *d*-spacing of 0.48 nm oriented along the <111> plane for the particle present within the shell confirmed the presence of NiFe<sub>2</sub>O<sub>4</sub>. Using NiFe<sub>2</sub>O<sub>4</sub> to Zr-precursor weight ratio of 1:10, monoparticulate core-shell morphology is evident with average shell thickness of 3.2 nm; however, at higher weight ratio of 1:25, multiple particles were observed inside a thicker shell of 6.1 nm. XRD of the CSNs prepared with NiFe<sub>2</sub>O<sub>4</sub> to Zr-precursor weight ratios of 1:5, 1:10 and 1:25 indicated nominal phase composition of NiFe<sub>2</sub>O<sub>4</sub> (95.7 wt.%)/ ZrO<sub>2</sub> (4.3 wt.%), NiFe<sub>2</sub>O<sub>4</sub> (91.2 wt.%)/ ZrO<sub>2</sub> (8.8 wt.%) and NiFe<sub>2</sub>O<sub>4</sub> (73.8 wt.%)/ ZrO<sub>2</sub> (26.2 wt.%), respectively. Among these materials, NiFe<sub>2</sub>O<sub>4</sub> (91.2 wt.%)/ ZrO<sub>2</sub> (8.8 wt.%) CSNs show stable average hydrogen and oxygen volume generation of 7.28 ml/g/cycle and 3.75 ml/g/cycle, respectively, at thermochemical reaction temperatures of 900°-1100 °C. Transient hydrogen profiles obtained for the NiFe<sub>2</sub>O<sub>4</sub> (91.2 wt.%)/ ZrO<sub>2</sub> (8.8 wt.%) CSNs at water splitting temperature of 900 °C show relatively stable hydrogen generation of 7.3 ml/g, 7.24 ml/g, 7.28 ml/g, and 7.3 ml/g during 2<sup>nd</sup>, 3<sup>rd</sup>, 4<sup>th</sup> and 5<sup>th</sup> thermochemical cycles, respectively. For these CSNs, average hydrogen volume generation rate of 0.087 ml/min/g/cycle was observed with oxygen volume generation rate of 0.038 ml/min/g/cycle during 5 consecutive thermochemical cycles.

## Acknowledgement

The authors gratefully acknowledge the financial support from the National Science Foundation, Grant number CBET#1134570 and Chemical and Biological Engineering department at South Dakota School of Mines & Technology.

## References

1. Chaudhuri RG, Parija S. 2012. Core/shell nanoparticles: classes, properties, synthesis mechanisms, characterization, and applications. *Chem Rev* 112(4): 2373-2433. <https://doi.org/10.1021/cr100449n>
2. Gawande MB, Goswami A, Asefa T, Guo H, Biradar AV, et al. 2015. Core-shell nanoparticles: synthesis and applications in catalysis and electrocatalysis. *Chem Soc Rev* 44(21): 7540-7590. <https://doi.org/10.1039/c5cs00343a>
3. Song X, Chen S, Guo L, Sun Y, Li X, et al. 2018. General dimension-controlled synthesis of hollow carbon embedded with metal single atoms or core-shell nanoparticles for energy storage applications. *Adv Energy Mater* 8(27): 1801101. <https://doi.org/10.1002/aenm.201801101>
4. Chatterjee K, Sarkar S, Rao KJ, Paria S. 2014. Core/shell nanoparticles in biomedical applications. *Adv Colloid Interface Sci* 209: 8-39. <https://doi.org/10.1016/j.cis.2013.12.008>
5. Mandl M, Wang X, Schimpke T, Kölper C, Binder M, et al. 2013. Group III nitride core-shell nano and microrods for optoelectronic applications. *Phys Status Solidi-R* 7(10): 800-814. <https://doi.org/10.1002/pssr.201307250>
6. Chen G, Ohulchanskyy TY, Liu S, Law W-C, Wu F, et al. 2012. Core/shell NaGdF<sub>4</sub>: Nd<sup>3+</sup>/NaGdF<sub>4</sub> nanocrystals with efficient near-infrared to near-infrared downconversion photoluminescence for bioimaging applications. *ACS Nano* 6(4): 2969-2977. <https://doi.org/10.1021/nn2042362>
7. Lal S, Link S, Halas NJ. 2007. Nano-optics from sensing to waveguiding. *Nat Photonics* 1(11): 641-648. <https://doi.org/10.1038/nphoton.2007.223>
8. El-Khatib KM, Hameed RMA, Amin RS, Fetohi AE. 2019. Core-shell structure Pt-transition metals nanoparticles supported on activated carbon for direct methanol fuel cells. *Microchem J* 145: 566-577. <https://doi.org/10.1016/j.microc.2018.11.020>
9. Rai P. 2019. Plasmonic noble metal@metal oxide core-shell nanoparticles for dye-sensitized solar cell applications. *Sustain Energy Fuels* 3(1): 63-91. <https://doi.org/10.1039/c8se00336j>
10. Misra RDK. 2010. Core-shell magnetic nanoparticle carrier for targeted drug delivery: challenges and design. *Mater Technol* 25(3-4): 118-126. <https://doi.org/10.1179/175355510x12723642365241>
11. Yang, G., Ding, H., Feng, J., Hao, Q., Sun, S, et al. 2017. Highly performance core-shell tio2 (b)/anatase homojunction nanobelts with active cobalt phosphide cocatalyst for hydrogen production. *Sci Rep* 7(1): 1-9. <https://doi.org/10.1038/s41598-017-15134-w>
12. Fang X, Wang J, Yu Y, Kang S, Cui L. 2020. Self-assembled CdS@BN core-shell photocatalysts for efficient visible-light-driven photocatalytic hydrogen evolution. *Int J Hydrog Energy* 45(29): 14841-14848. <https://doi.org/10.1016/j.ijhydene.2020.03.199>
13. Preethi V, Kanmani S. 2014. Photocatalytic hydrogen production using Fe<sub>2</sub>O<sub>3</sub>-based core shell nano particles with ZnS and CdS. *Int J Hydrog Energy* 39(4): 1613-1622. <https://doi.org/10.1016/j.ijhydene.2013.11.029>
14. Guo X, Peng Y, Liu G, Xie G, Guo Y, et al. 2020. An efficient ZnIn<sub>2</sub>S<sub>4</sub>@CuInS<sub>2</sub> core-shell p-n heterojunction to boost visible-light photocatalytic hydrogen evolution. *J Phys Chem C* 124(11): 5934-5943. <https://doi.org/10.1021/acs.jpcc.9b11623>
15. Amar VS, Puszynski JA, Shende RV. 2015. H<sub>2</sub> generation from thermochemical water-splitting using yttria stabilized NiFe<sub>2</sub>O<sub>4</sub> core-shell nanoparticles. *J Renew Sustain Ener* 7(2):023113. <https://doi.org/10.1063/1.4915312>
16. Bhosale RR, Shende RV, Puszynski JA. 2010. H<sub>2</sub> generation from thermochemical water-splitting using sol-gel synthesized ferrites (MXFeYOZ, M = Ni, Zn, Sn, Co, Mn, Ce). In Proceedings of 2010 AIChE Annual Meeting.
17. Bhosale R, Khadka R, Puszynski J, Shende R. 2011. H<sub>2</sub> generation from two-step thermochemical water-splitting reaction using sol-gel derived SnxFeyOz. *J Renew Sustain Ener* 3(6):063104. <https://doi.org/10.1063/1.3659684>
18. Bhosale RR, Shende RV, Puszynski JA. 2011. Synthesis of nano-sized ferrite materials for H<sub>2</sub> generation from high temperature water-splitting reaction. In Proceedings of NSTI-Nanotech Conference & Expo 237-240.
19. Bhosale R, Kumar A, AlMamani F, Ghosh U, Saad Anis MS, et al. 2016. Solar hydrogen production via a samarium oxide-based thermochemical water splitting cycle. *Energies* 9(5):316. <https://doi.org/10.3390/en9050316>
20. Bhosale RR, Yousefi S, Folady J, Jilani M, Dardor D, et al. 2015. Thermodynamic analysis of solar fuel production via thermochemical H<sub>2</sub>O and/or CO<sub>2</sub> splitting using tin oxide based redox reactions. In Proceedings of the 4th International Gas Processing Symposium 39-48. <https://doi.org/10.1016/b978-0-444-63461-0.50004-3>

21. Walters I, Shende R, Puszynski JA. 2014. Hydrogen Production from thermochemical water-splitting using ferrites prepared by solution combustion synthesis. *Adv Sci Technol* 91: 32-38. <https://doi.org/10.4028/www.scientific.net/ast.91.32>
22. Bhosale RR, Shende RV, Puszynski JA. 2012. Thermochemical water-splitting for H<sub>2</sub> generation using sol-gel derived Mn-ferrite in a packed bed reactor. *Int J Hydrog Energy* 37(3):2924-2934. <https://doi.org/10.1016/j.ijhydene.2011.03.010>
23. Safari F, Dincer I. A review and comparative evaluation of thermochemical water splitting cycles for hydrogen production. *Energy Convers Manag* 205: 112182. <https://doi.org/10.1016/j.enconman.2019.112182>
24. Zhai S, Rojas J, Ahlborg N, Lim K, Toney MF, et al. 2018. The use of poly-cation oxides to lower the temperature of two-step thermochemical water splitting. *Energy Environ Sci* 11(8):2172-2178. <https://doi.org/10.1039/c8ee00050f>
25. Goikoetxea NB, Gómez-Mancebo MB, Fernández-Saavedra R, Borlaf F, García-Pérez F, et al. Understanding water-splitting thermochemical cycles based on nickel and cobalt ferrites for hydrogen production. *Int J Hydrog Energy* 44(33): 17578- 17585. <https://doi.org/10.1016/j.ijhydene.2019.05.003>
26. Goikoetxea NB, Gómez-Mancebo MB, Fernández-Saavedra R, García-Pérez F, Jiménez JA, et al. Study of the performance of Co and Ni ferrites after several cycles involved in watersplitting thermochemical cycles. *Int J Hydrog Energy* 41(38): 16696-16704. <https://doi.org/10.1016/j.ijhydene.2016.07.085>
27. Pasala X, Bhosale RR, Amar VS, Puszynski JA, Shende RV, "Thermally stabilized ferrite nanoparticles for hydrogen generation from thermochemical water- splitting reaction." In Proceedings of 2012 AIChE Annual Meeting. 2012.
28. Amar VS, Shende RV. 2018. "Core-shell nanoscale ferrite for thermochemical hydrogen generation." In Proceedings of TechConnect Briefs-Materials for Energy Efficiency and Sustainability 13-16.
29. Moradi R, Groth KM. 2019. Hydrogen storage and delivery: Review of the state of the art technologies and risk and reliability analysis. *Int J Hydrog Energy* 44(23): 12254-12269. <https://doi.org/10.1016/j.ijhydene.2019.03.041>
30. Chanchetti LF, Leiva DR, de Faria LIL, Ishikawa TT. 2020. A scientometric review of research in hydrogen storage materials. *Int J Hydrog Energy* 45(8): 5356-5366. <https://doi.org/10.1016/j.ijhydene.2019.06.093>
31. Eriksson ELV, Gray EMA. 2017. Optimization and integration of hybrid renewable energy hydrogen fuel cell energy systems- a critical review. *Appl Energy* 202: 348-364. <https://doi.org/10.1016/j.apenergy.2017.03.132>
32. Scheffe JR, Li J, Weimer AW. 2010. A spinel ferrite/hercynite water-splitting redox cycle. *Int J Hydrog Energy* 35(8): 3333-3340. <https://doi.org/10.1016/j.ijhydene.2010.01.140>
33. Al-Shankiti IA, Bayon A, Weimer AW. Reduction kinetics of hercynite redox materials for solar thermochemical water splitting. *Chem Eng J* 389: 124429. <https://doi.org/10.1016/j.cej.2020.124429>
34. Villafán-Vidales HI, Arancibia-Bulnes CA, Valades-Pelayo PJ, Romero-Paredes H, Cuentas-Gallegos AK, et al. Hydrogen from solar thermal energy. *Solar Hydrog Prod* 319-363. <https://doi.org/10.1016/b978-0-12-814853-2.00010-2>
35. Amar VS, Puszynski JA, Shende RV. 2019. Thermally stabilized redox materials and applications thereof. US Patent 20190206599.
36. Bhosale RR, Shende RV, Opoku MK, Puszynski JA. 2009. H<sub>2</sub> generation from water-splitting using novel ferrite foam materials. In Proceedings of AIChE Annual Meeting.
37. Shende RV, Puszynski JA, Opoku MK, Bhosale RR. 2009. Synthesis of novel ferrite foam material for water-splitting application. In Proceedings of NSTI– Nanotech Conference.
38. Amar VS. 2017. Hydrogen Generation from Thermochemical Water-splitting Process Using Thermally Stabilized Redox Materials. Ph. D Thesis, South Dakota School of Mines and Technology, USA.
39. Muhich CL, Evanko BW, Weston KC, Lichty P, Liang X, et al. 2013. Efficient generation of H<sub>2</sub> by splitting water with an isothermal redox cycle. *Science* 341(6145): 540-542. <https://doi.org/10.1126/science.1239454>
40. Steinfeld A. 2002. Solar hydrogen production via a two-step water-splitting thermochemical cycle based on Zn/ZnO redox reactions. *Int J Hydrog Energy* 27: 611-619.
41. Chueh WC, Falter C, Abbott M, Scipio D, Furler P, et al. 2010. High-flux solar-driven thermochemical dissociation of CO<sub>2</sub> and H<sub>2</sub>O using nonstoichiometric ceria. *Science* 330(6012):1797-1801. <https://doi.org/10.1126/science.1197834>
42. Fresno F, Fernández-Saavedra R, Gómez-Mancebo MB, Vidal A, Sánchez M, et al. 2009. Solar hydrogen production by two- step thermochemical cycles: evaluation of the activity of commercial ferrites. *Int J Hydrog Energy* 34(7): 2918-2924. <https://doi.org/10.1016/j.ijhydene.2009.02.020>
43. Scheffe JR, Allendorf MD, Coker EN, Jacobs BW, McDaniel AH, et al. 2011. Hydrogen production via chemical looping redox cycles using atomic layer deposition-synthesized ironoxide and cobalt ferrites. *Chem Mater* 23(8): 2030-2038. <https://doi.org/10.1021/cm103622e>
44. Tamaura Y, Kojima N, Hasegawa N, Inoue M, Uehara R, Gokon N, et al. 2001. Stoichiometric studies of H<sub>2</sub> generation reaction for H<sub>2</sub>O/Zn/Fe<sub>3</sub>O<sub>4</sub> system. *Int J Hydrog Energy* 26(9):917-922. [https://doi.org/10.1016/s0360-3199\(01\)00039-8](https://doi.org/10.1016/s0360-3199(01)00039-8)
45. Kaneko H, Kodama T, Gokon N, Tamaura Y, Lovegrove K, et al. 2004. Decomposition of Zn-ferrite for O<sub>2</sub> generation by concentrated solar radiation. *Solar Energy* 76(1-3): 317-322. <https://doi.org/10.1016/j.solener.2003.08.034>
46. Amar VS, Puszynski JA, Shende RV. 2015. H<sub>2</sub> generation from thermochemical water-splitting using core-shell ni-ferrite nanoparticles. *Cleantech Proceedings* 2014: 139-142. <https://doi.org/10.1063/1.4915312>
47. Bhosale RR, Shende RV, Puszynski JA. 2012. Thermochemical water-splitting for H<sub>2</sub> generation using sol-gel derived Mn-ferrite in a packed bed reactor. *International Journal of Hydrogen Energy* 37(3): 2924-2934. <https://doi.org/10.1016/j.ijhydene.2011.03.010>
48. Bhosale RR, Shende RV, Puszynski JA. 2012. Sol-gel synthesis of ferrite foam materials for H<sub>2</sub> generation from water-splitting reaction. In Proceedings of NSTI– Nanotech Conference & Expo.
49. Bhosale RR, Khadka R, Quickel S, Shende RV, Puszynski JA. 2010. Sol-gel derived Sn-ferrite for H<sub>2</sub> generation from water splitting reaction. In Proceedings of South Dakota Academy of Science Annual Meeting, USA.
50. Amar VS, Pasala XM, Puszynski JA, Shende RV. 2015. Sonication derived powdered mixtures of ferrite and ceramic nanoparticles for H<sub>2</sub> generation. *Am J Energy Res* 3(2): 25-31. <https://doi.org/10.12691/ajer-3-2-2>
51. Seong S, Park I-S, Jung YC, Lee T, Kim SY, et al. 2019. Synthesis of Ag-ZnO core-shell nanoparticles with enhanced photocatalytic activity through atomic layer deposition. *Mat Des* 177: 107831. <https://doi.org/10.1016/j.matdes.2019.107831>

52. Yang H, Chen Y, Qin Y. 2020. Application of atomic layer deposition in fabricating high-efficiency electrocatalysts. *Chinese J Catal* 41(2): 227- 241. [https://doi.org/10.1016/s1872-2067\(19\)63440-6](https://doi.org/10.1016/s1872-2067(19)63440-6)
53. Amar VS, Puszynski JA, Shende RV. 2014. Hydrogen generation from thermochemical water-splitting using core-shell ni-ferrite nanoparticles. *Cleantech Proceedings 2014*: 139-142.
54. Angotzi MS Musinu A, Mameli V, Ardu A, Cara C, et al. 2017. Spinel ferrite core-shell nanostructures by a versatile solvothermal seed-mediated growth approach and study of their nanointerfaces. *ACS nano* 11(8): 7889-7900. <https://doi.org/10.1021/acsnano.7b02349>
55. Jian G, Zhang C, Yan C, Moon KS, Wong CP. 2018. Scalable preparation of fully coated Ag@ BaTiO<sub>3</sub> core@ shell particles via poly (vinylpyrrolidone) assistance for high-k applications. *ACS Applied Nano Materials* 1(3): 1396-1405. <https://doi.org/10.1021/acsnm.8b00220>
56. Silva RM, Raimundo RA, Fernandes WV, Torres SM, Silva VD, et al. 2018. Proteic sol-gel synthesis, structure and magnetic properties of Ni/NiO core-shell powders. *Ceramics International* 44(6): 6152-6156. <https://doi.org/10.1016/j.ceramint.2017.12.248>
57. Vowinkel S, Schäfer CG, Cherkashinin G, Fasel C, Roth F, et al. 2016. 3D-ordered carbon materials by melt-shear organization for tailor-made hybrid core-shell polymer particle architectures. *J Mater Chem C* 4(18): 3976-3986. <https://doi.org/10.1039/c5tc03483c>
58. Rossinelli AA, Riedinger A, Marqués-Gallego P, Knüsel PN, Antolinez FV, et al. 2017. High-temperature growth of thick-shell CdSe/CdS core/shell nanoplatelets. *Chem Commun* 53(71): 9938-9941. <https://doi.org/10.1039/c7cc04503d>
59. Salinas D, Guerrero S, Campos CH, Bustamante TM, Pecchi G. 2020. The effect of the ZrO<sub>2</sub> loading in SiO<sub>2</sub>@ZrO<sub>2</sub>-CaO catalysts for transesterification reaction. *Materials (Basel)* 13(1): 221. <https://doi.org/10.3390/ma13010221>
60. Hussein AM, Shende RV. 2014. Enhanced hydrogen generation using ZrO<sub>2</sub>- modified coupled ZnO/TiO<sub>2</sub> nanocomposites in the absence of noble metal co- catalyst. *Int J Hydrog Energy* 39(11): 5557-5568. <https://doi.org/10.1016/j.ijhydene.2014.01.149>
61. Yoshimura M. 1950. Phase stability of zirconia. *Am Ceram Soc Bull* 67(12): 1950-1955.
62. Bhosale RR, Shende RV, Puszynski JA. 2010. H<sub>2</sub> generation from thermochemical water-splitting using sol-gel derived Ni-ferrite. *J Energy Power Eng* 4(6): 27-38.
63. Amar VS, Pasala XM, Puszynski JA, Shende RV. 2015. Sonication derived powdered mixtures of ferrite and ceramic nanoparticles for H<sub>2</sub> generation. *American Journal of Energy Research* 3(2): 25-31. <https://doi.org/10.12691/ajer-3-2-2>
64. Bhosale RR, Shende RV, Puszynski JA. 2012. Thermochemical water-splitting for H<sub>2</sub> generation using sol-gel derived Mn-ferrite in a packed bed reactor. *International Journal of Hydrogen Energy* 37(3): 2924-2934. <https://doi.org/10.1016/j.ijhydene.2011.03.010>
65. Bhosale RR, Shende RV, Puszynski JA. 2010. H<sub>2</sub> generation from thermochemical water-splitting using sol-gel synthesized Zn/Sn/Mn-doped Ni-ferrite. *International Review of Chemical Engineering* 2(7): 852-862.
66. Mercera PDL, Van Ommen JG, Doesburg EBM, Burggraaf AJ, Roes JRH. 1991. Stabilized tetragonal zirconium oxide as a support for catalysts Evolution of the texture and structure on calcination in static air. *Applied catal* 78(1): 79-96. [https://doi.org/10.1016/0166-9834\(91\)80090-j](https://doi.org/10.1016/0166-9834(91)80090-j)
67. Šepelák V, Bergmann I, Feldhoff A, Heitjans P, Krumeich F, et al. 2007. Nanocrystalline nickel ferrite, NiFe<sub>2</sub>O<sub>4</sub>: mechanosynthesis, nonequilibrium cation distribution, canted spin arrangement and magnetic behavior. *J Phys Chem C* 111(13): 5026-5033. <https://doi.org/10.1021/jp067620s>
68. Bhosale RR, Shende RV, Puszynski JA. 2012. Sol-gel derived NiFe<sub>2</sub>O<sub>4</sub> modified with ZrO<sub>2</sub> for hydrogen generation from solar thermochemical water-splitting reaction. *MRS proceedings* 1387. <https://doi.org/10.1557/opl.2012.772>
69. El-Fadl AA, Eltokhey AM, Abu-Sehley AA, El-Attar HM. 2018. Fabrication and analysis of the structural phase transition of ZrO<sub>2</sub> nanoparticles using modified facile sol-gel route. *Phase Transitions* 92(1): 36-51. <https://doi.org/10.1080/01411594.2018.1545904>
70. Huy DK, Duong NP, Loan TT, Chung HM, Thanh NK, et al. Synthesis and characterization of NiFe<sub>2</sub>O<sub>4</sub>/ZnO core-shell nanocomposites. *VNU J Sci Mathem-Phys* 34(4). <https://doi.org/10.25073/2588-1124/vnumap.4297>
71. Yang J, Ren J, Guo H, Qin X, Han B, et al. 2015. The growth of Ni<sub>n</sub> clusters and their interaction with cubic, monoclinic and tetragonal ZrO<sub>2</sub> surfaces-a theoretical and experimental study. *RSC advances* 5(74): 59935-59945. <https://doi.org/10.1039/c5ra07738a>
72. Possato LG, Pereira E, Gonçalves RGL, Pulcinelli SH, Martins L, et al. 2020. Controlling the porosity and crystallinity of MgO catalysts by addition of surfactant in the sol-gel synthesis. *Catal Today* 344: 52-58. <https://doi.org/10.1016/j.cattod.2018.10.027>
73. Dhaneswara D, Sofyan N. 2016. Effect of different Pluronic P123 triblock copolymer surfactant concentrations on SBA-15 pore formation. *Int J Technol* 7(6): (2016): 1009. <https://doi.org/10.14716/ijtech.v7i6.3412>
74. Suhendi A, Nandiyanto ABD, Ogi T, Okuyama K. 2013. Agglomeration-free core-shell polystyrene/silica particles preparation using an electrospray method and additive-free cationic polystyrene core. *Mater Let* 91: 161-164. <https://doi.org/10.1016/j.matlet.2012.09.041>
75. Long NV, Thi CM, Nogami M, Ohtaki M. 2012. Novel issues of morphology, size and structure of Pt nanoparticles in chemical engineering: surface attachment, aggregation or agglomeration, assembly and structural changes. *New J Chem* 36(6): 1320. <https://doi.org/10.1039/c2nj40027h>
76. Gonzales M, Krishnan KM. Phase transfer of highly monodisperse iron oxide nanocrystals with Pluronic F127 for biomedical applications. *J Magn Magn Mater* 311(1): 59-62. <https://doi.org/10.1016/j.jmmm.2006.10.1150>
77. Chang LC, Chang YY, Gau CS. Interfacial properties of Pluronics and the interactions between Pluronics and cholesterol/DPPC mixed monolayers. *J Colloid and Interface Sci* 322(1): 263-273. <https://doi.org/10.1016/j.jcis.2008.02.051>
78. Tamura Y, Kojima M, Sano T, Ueda Y, Hasegawa N, et al. 1998. Thermodynamic evaluation of water splitting by a cation-excessive (Ni, Mn) ferrite. *Int J Hydrog Energy* 23(12): 1185-1191. [https://doi.org/10.1016/s0360-3199\(98\)00007-x](https://doi.org/10.1016/s0360-3199(98)00007-x)
79. Han SB, Kang TB, Joo OS, Jung KD. 2007. Water splitting for hydrogen production with ferrites. *Solar Energy* 81(5): 623-628. <https://doi.org/10.1016/j.solener.2006.08.012>
80. Fernández-Saavedra R, Gómez-Mancebo MB, Caravaca C, Sánchez M, Quejido AJ, et al. 2014. Hydrogen production by two-step thermochemical cycles based on commercial nickel ferrite: kinetic and structural study. *Int J Hydrog Energy* 39(13): 6819-6826. <https://doi.org/10.1016/j.ijhydene.2014.02.076>
81. Zabetto FL, Gualdi AJ, Eiras JA, de Oliveira AJA, Garcia D. 2012. Influence of the sintering temperature on the magnetic and electric properties of NiFe<sub>2</sub>O<sub>4</sub> ferrites. *Mater Res* 15(3): 428-433. <https://doi.org/10.1590/s1516-14392012005000043>
82. Islam R, Rahman MO, Hakim MA, Saha DK, Saiduzzaman S, et al. 2012. Effect of sintering temperature on structural and magnetic properties of Ni<sub>0.55</sub>Zn<sub>0.45</sub>Fe<sub>2</sub>O<sub>4</sub> ferrites. *Mater Sci Applicat* 3(5): 326-331. <https://doi.org/10.4236/msa.2012.35048>